Modeling suggests that oblique extension facilitates rifting and continental break-up

Sascha Brune,[1] Anton A. Popov,[1,2] and Stephan V. Sobolev[1]

Received 12 September 2011; revised 27 March 2012; accepted 5 June 2012; published 2 August 2012.

[1] In many cases the initial stage of continental break-up was and is associated with oblique rifting. That includes break-up in the Southern and Equatorial Atlantic, separation from eastern and western Gondwana as well as many recent rift systems, like Gulf of California, Ethiopia Rift and Dead Sea fault. Using a simple analytic mechanical model and advanced numerical, thermomechanical modeling techniques we investigate the influence of oblique extension on the required tectonic force in a three-dimensional setting. While magmatic processes have been already suggested to affect rift evolution, we show that additional mechanisms emerge due to the three-dimensionality of an extensional system. Focusing on non-magmatic rift settings, we find that oblique extension significantly facilitates the rift process. This is due to the fact that oblique deformation requires less force in order to reach the plastic yield limit than rift-perpendicular extension. The model shows that in the case of two competing non-magmatic rifts, with one perpendicular and one oblique to the direction of extension but otherwise having identical properties, the oblique rift zone is mechanically preferred and thus attracts more strain.

Citation: Brune, S., A. A. Popov, and S. V. Sobolev (2012), Modeling suggests that oblique extension facilitates rifting and continental break-up, *J. Geophys. Res.*, *117*, B08402, doi:10.1029/2011JB008860.

1. Introduction

[2] Rifting and continental break-up belong to the fundamental features of plate tectonics. Continental rifting has been studied extensively using mathematical models [e.g., *McKenzie*, 1978; *Royden and Keen*, 1980; *Braun and Beaumont*, 1989; *Huismans and Beaumont*, 2003; *Regenauer-Lieb et al.*, 2008; *Huismans and Beaumont*, 2011]; however, the conditions which allow rifting to result in continental break-up remain poorly understood. Several mechanism exist that are thought to facilitate break-up: Inherited weak zones originate from the amalgamation of distinct tectonic plates that are reactivated by the rift process [*Ziegler and Cloetingh*, 2004]. Stress focusing occurs when break-up does not take place simultaneously in a rift zone, but propagates in a certain direction, as was the case for the opening of the South Atlantic [*Torsvik et al.*, 2009]. Melt generation and magma transport weaken the lithosphere both by efficient heating, and by mechanical strength reduction [*Buck*, 2007]. The impingement of mantle plumes on active rift zones plays an important role in triggering continental break-up [*Ziegler and Cloetingh*, 2004]. Here we focus at another possible rift-intensifying process that was to our knowledge never discussed in this aspect in the literature: extension with a direction that is strongly oblique to the rift axis.

[3] Oblique rifting was associated with break-up at many places in the world (Figure 1). The separation of Africa and South America featured significantly oblique separation angles [*Nürnberg and Müller*, 1991; *Macdonald et al.*, 2003; *Torsvik et al.*, 2009; *Moulin et al.*, 2010], especially the North Falkland-South African section [*Parsiegla et al.*, 2009] and the Equatorial Atlantic [*Edwards et al.*, 1997]. In the Indian Ocean region, oblique break-up separated Africa and Madagascar [*de Wit*, 2003], Madagascar and India [*Storey et al.*, 1995], Sri Lanka and South India from Antarctica [*Gaina et al.*, 2007], Antarctica and Australia [*Whittaker et al.*, 2007], opened the Gulf of Aden [*Bellahsen et al.*, 2003] and the Red Sea [*Hempton*, 1987]. In the North Atlantic, the formation of the Davis Strait involved highly oblique rifting [*Suckro et al.*, 2012] while the Fram Strait separates two sheared conjugate margins [*Engen et al.*, 2008]. Moreover, several currently active rifts exhibit an oblique component, like in the Gulf of California [*Lizarralde et al.*, 2007], the Dead Sea Fault [*Weber et al.*, 2009], and the Ethiopian Rift [*Corti*, 2008]. The locus and the orientation of a developing rift zone is controlled by the complex interplay of tectonic forces, lithospheric inheritance and overall plate geometry. The impact of individual contributions from e.g. slab pull, mantle drag, inherited faults, mantle anisotropy and rift orientation strongly depend on individual plate configurations and are often poorly known. Thus, it can not be excluded that some or all of the rifts mentioned before are oblique because the tectonic system simply had no other

[1]Geodynamic Modelling Section, Helmholtz Centre Potsdam, GFZ German Research Centre for Geosciences, Potsdam, Germany.

[2]Now at Institute of Geosciences, Johannes Gutenberg University Mainz, D-55099 Mainz, Germany.

Corresponding author: S. Brune, Geodynamic Modelling Section, Helmholtz Centre Potsdam, GFZ German Research Centre for Geosciences, Telegrafenberg, Potsdam D-14473, Germany. (brune@gfz-potsdam.de)

0148-0227/12/2011JB008860

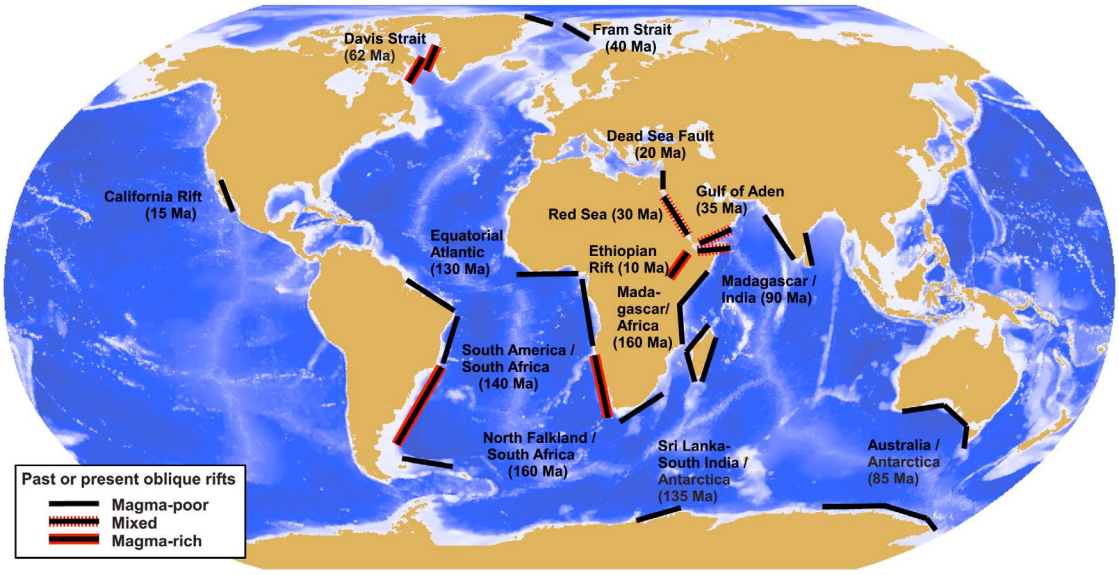

Figure 1. Worldwide compilation of obliquely rifted conjugate margins and presently active oblique rifts. Numbers indicate approximate times of rift initiation. Magma-rich margins and rifts are indicated in red. If some segments of the same rift are magma-rich and others magma-poor the rift type is designated as mixed (for references see text).

choice. Keeping this in mind, this study shows that oblique rift zones require less tectonic force than perpendicular rifts so that plate motions involving significant rift obliquity appear to be mechanically preferred.

[4] Many analog experiments successfully addressed the topic of continental rifting and the fault patterns caused by oblique extension [*Withjack and Jamison*, 1986; *Tron and Brun*, 1991; *Clifton et al.*, 2000; *Chemenda et al.*, 2002; *Corti et al.*, 2003; *Sokoutis et al.*, 2007; *Autin et al.*, 2010]. The advantage of analog models is that they are three-dimensional by default so that oblique rift models are relatively straightforward to obtain. However, analog models necessitate important simplifications, particularly realistic elasto-visco-plastic rheology and temperature dependency are hard to implement. While present-day numerical codes include these features, models of oblique rifting intrinsically require computationally expensive calculations in three dimensions which is why only two numerical model have been published to our knowledge so far [*van Wijk*, 2005; *Allken et al.*, 2011]. Neither analog nor numerical publications, however, addressed the impact of rift obliquity on the tectonic force that is required to allow extension.

[5] In this study, we investigate how oblique rifting influences the effective strength of the lithosphere. To this aim, we first conduct simplified analytic modeling followed by three-dimensional numerical experiments that comprise a layered lithosphere of elasto-visco-plastic, stress- and temperature-dependent rheology. Presenting two distinct numerical model setups, we induce obliqueness by applying boundary velocities that are not perpendicular to the prospective rift zone. In the first setup, we compute the force required to maintain a certain rift velocity and evaluate its dependency on the extensional direction. In the other setting, two possible rift zones of different angles evolve under uniform extension. Finally, we apply dynamic boundary condition by prescribing boundary forces and observe the kinematic behavior of the system. In all cases, we find that oblique rifting is preferred.

2. Analytical Considerations

[6] Fundamental insights can be drawn from an analytical solution of a simplified formulation of the problem. We therefore consider a homogeneous and isotropic plate to consist of a linearly elastic material that becomes perfectly plastic when von Mises yield stress is reached. Gravity is neglected. The plate is deformed by displacing the plate edge by the distance u in a direction defined by the angle of obliquity α (Figure 2a).

[7] We build our analytics on the work of *Withjack and Jamison* [1986] who solved the elastic part of the problem, i.e. stress as a function of displacement. Note that they used the notation that tensile stresses are positive, while we apply the geophysical notation where compressive stresses have positive sign. Furthermore, their definition of α is opposite to ours, so that our α equals to 90° minus theirs. The solution of *Withjack and Jamison* [1986] in the principal coordinate system yields two horizontal stresses

$$\sigma_{H1} = -\frac{E}{2}\frac{u}{L_x}\left[\frac{1}{1-\nu}\cos(\alpha) + \frac{1}{1+\nu}\right] \quad (1)$$

$$\sigma_{H2} = -\frac{E}{2}\frac{u}{L_x}\left[\frac{1}{1-\nu}\cos(\alpha) - \frac{1}{1+\nu}\right] \quad (2)$$

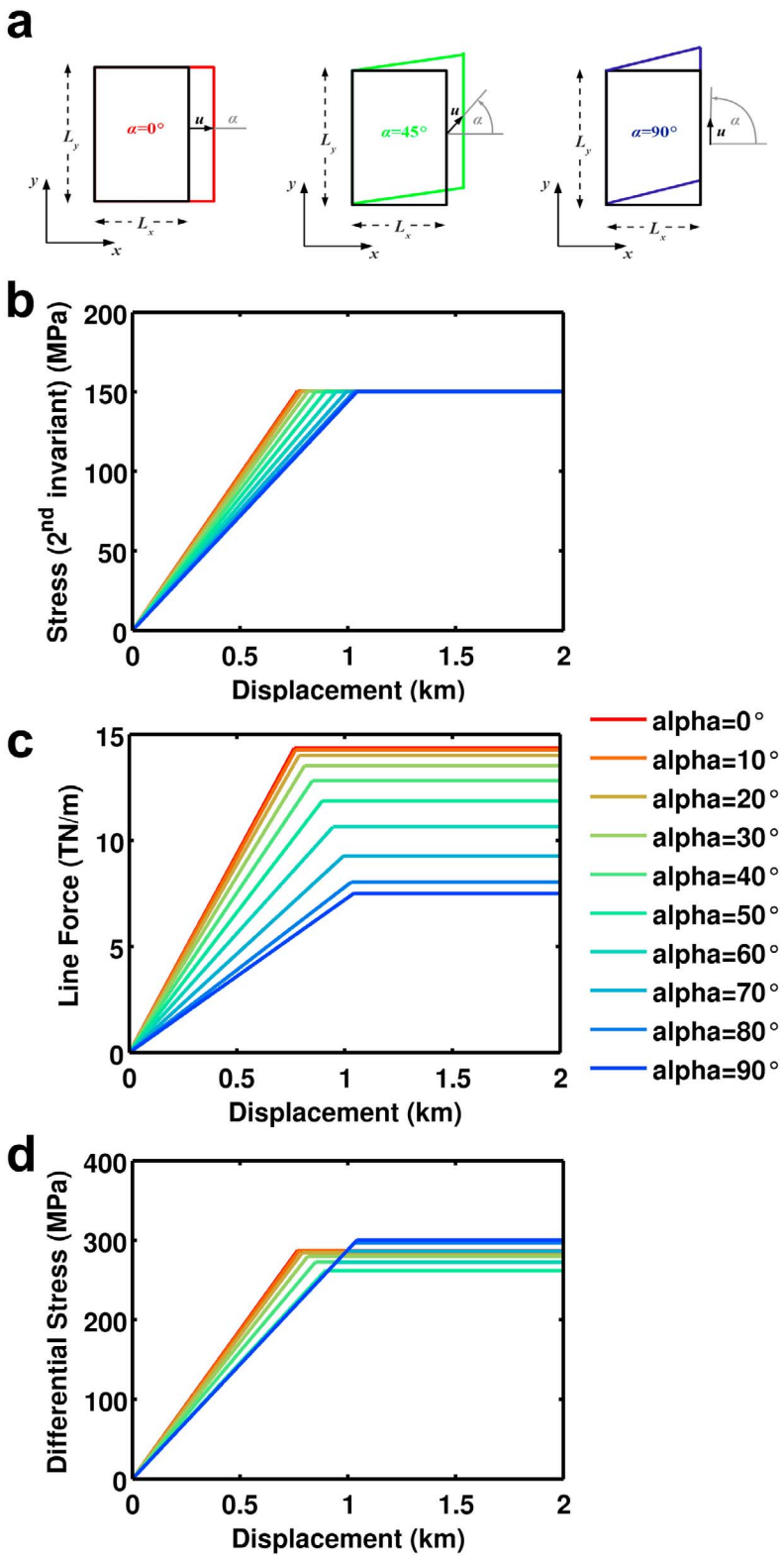

Figure 2. (a) Analytical setup and (b–d) solutions using upper crustal elastic parameters as shown in Table 1 (Young's modulus $E = \frac{9KG}{3K+G} = 88.6$ GPa, Poisson ratio $\nu = \frac{3K-2G}{2(3K+G)} = 0.23$).

and the vertical stress

$$\sigma_V = \sigma_{zz} = 0 \tag{3}$$

at which our notation is used and E is the Young's modulus, v the Poisson ratio, u displacement and L_x the length of the model domain in x-direction.

[8] We compute the individual components of the stress tensor σ_{ij} in the xyz-coordinate system by classical rotational coordinate transformation.

$$\sigma_{xx} = -\frac{Eu}{L_x}\cos\alpha\frac{1}{1-\nu^2} \tag{4}$$

$$\sigma_{yy} = -\frac{Eu}{L_x}\cos\alpha\frac{\nu}{1-\nu^2} \tag{5}$$

$$\sigma_{zz} = 0 \tag{6}$$

$$\sigma_{xy} = -\frac{1}{2}\frac{Eu}{L_x}\sin\alpha\frac{1}{1+\nu} \tag{7}$$

$$\sigma_{xz} = 0 \tag{8}$$

$$\sigma_{yz} = 0 \tag{9}$$

Based on σ_{ij}, we evaluate the second invariant of deviatoric stress tensor τ_{II}:

$$\tau_{II} = \sqrt{\frac{1}{2}(\sigma_{xx}-p)^2 + \frac{1}{2}(\sigma_{yy}-p)^2 + \frac{1}{2}(\sigma_{zz}-p)^2 + \sigma_{xy}^2 + \sigma_{xz}^2 + \sigma_{yz}^2} \tag{10}$$

with pressure

$$p = \frac{1}{3}(\sigma_{xx} + \sigma_{yy} + \sigma_{zz}). \tag{11}$$

[9] Since τ_{II} depends on the displacement u via the stress tensor, we can compute the critical displacement u_{yield} that is required to reach von Mises yield stress τ_{yield}:

$$\tau_{II}(u_{yield}) = \tau_{yield}. \tag{12}$$

[10] Finally, we evaluate the line force F at the displaced plate edge that has to be applied in order to realize the given displacement. This force results from Pythagorean addition of the stress components facing in x-direction:

$$F(u) = \sqrt{\sigma_{xx}^2 + \sigma_{xy}^2 + \sigma_{xz}^2}\cdot L_z. \tag{13}$$

[11] This formula holds true, since the vertical stress σ_{zz} vanishes. If this was not the case, computed tectonic forces would have to be corrected for the vertical stress component as discussed in section 4.1 (see equation (31)). Applying equations (4), (7), and (8) and setting u to u_{yield} results in the force at the plastic limit:

$$F_{yield} = \tau_{yield}L_z\sqrt{\frac{\cos^2\alpha + \frac{1}{4}\sin^2\alpha(1-\nu)^2}{\frac{1}{3}\cos^2\alpha(\nu^2-\nu+1) + \frac{1}{4}\sin^2\alpha(1-\nu)^2}}. \tag{14}$$

[12] A similar solution can be obtained if we do not consider an elastic material, but an incompressible viscous fluid. By using the analogy of linear viscous flow and elastic deformation we assume in equations (1) to (13) a Poisson ratio of $\nu = 0.5$ (incompressibility) and we substitute displacements u by velocities $\dot{u}$ as well as the shear modulus G by viscosity η (note that $E = 2G(1+\nu)$ must be replaced by 3η). In this case, the force at plastic yield will be given by the simple relation:

$$F_{yield} = \tau_{yield}L_z\sqrt{\frac{1+15\cos^2\alpha}{1+3\cos^2\alpha}}. \tag{15}$$

[13] From the more general equation (14), we derive two end-member cases, i.e. strike-slip ($\alpha = 90^\circ$) and pure extension ($\alpha = 0^\circ$) with fairly simple expressions:

$$F_{strike-slip} = \tau_{yield}L_z \tag{16}$$

and

$$F_{extension} = \frac{\tau_{yield}L_z}{\sqrt{\frac{1}{3}(\nu^2-\nu+1)}}. \tag{17}$$

[14] In the visco-plastic limit and for incompressible elastic materials, equation (16) does not change while equation (17) simplifies to:

$$F_{extension} = 2\tau_{yield}L_z. \tag{18}$$

[15] The ratio of $F_{extension}$ to $F_{strike\text{-}slip}$ is exactly 2 for incompressible media where the Poisson ratio ν is 0.5. For more realistic materials with $\nu \approx 0.25$, the force ratio amounts to 1.9. Hence, it is a general feature of Earth-relevant elasto-plastic and visco-plastic materials that the yield force is ~2 times higher for pure extension than for strike-slip.

[16] We plot the analytical solutions of the problem's key variables τ_{II}, F, and $\sigma_1 - \sigma_3$ in Figure 2. We thereby use upper crustal values for the elastic parameters (see Table 1), a realistic value for von Mises yield stress ($\tau_{yield} \sim$ 150 MPa), a model width L_x of 250 km and identify L_z with the depth of typical brittle-ductile transition in the mantle (50 km). During elastic deformation, all variables increase linearly with displacement. Plastic deformation commences when τ_{II} reaches τ_{yield} and is characterized by constant values for the considered variables. Note that for pure extension, the yield limit is reached with least displacement. The tectonic force F depends non-linearly on α showing clearly that oblique extension is favored mechanically over perpendicular extension.

[17] From the classical fault mechanics point of view this result seems counterintuitive, since strike-slip motion is an intermediate case between extension and compression, with compression requiring highest and extension least differential stress [e.g., *Sibson*, 1974]. The apparent contradiction however resolves when we compute the differential stress $\sigma_1 - \sigma_3$ in the plastic deformation phase. The smallest principal stress σ_3 is equal to σ_{H1} of equation (1) as it is negative (tensile) and smaller than both σ_{H2} and σ_V for all α. The largest principal stress σ_1 can be identified with σ_{H2} which is positive (compressive) if α exceeds a certain critical

Table 1. Parameters[a]

Parameter	Upper Crust	Lower Crust	Strong Mantle	Weak Mantle
Density, ρ (kg m^{-3})	2700	2850	3300	3300
Thermal expansivity, α (10^{-5} K^{-1})	2.7	2.7	3.0	3.0
Bulk modulus, K (GPa)	55	63	122	122
Shear modulus, G (GPa)	36	40	74	74
Heat capacity, C_p (J kg^{-1} K^{-1})	1200	1200	1200	1200
Heat conductivity, λ (W K^{-1} m^{-1})	2.5	2.5	3.3	3.3
Radiogenic heat production, A (μW m^{-3})	1.3	0.2	0	0
Initial friction coefficient, μ (-)	0.6	0.6	0.6	0.6
Maximum plastic friction softening[b]	90 %	90%	none	none
Cohesion, c (MPa)	5.0	5.0	5.0	5.0
Pre-exponential constant for diffusion creep, log(B_{Diff}) (Pa^{-1} s^{-1})	-	-	−8.65	−8.65
Activation energy for diffusion creep, E_{Diff} (kJ mol^{-1})	-	-	375	335
Activation volume for diffusion creep, V_{Diff} (10^{-6} m^3/mol)	-	-	6	4
Pre-exponential constant for dislocation, creep , log(B_{Disloc}) (Pa^{-n} s^{-1})	−28.0	−21.05	−15.56	−15.05
Power law exponent for dislocation, creep, n	4.0	4.2	3.5	3.5
Activation energy for dislocation creep, E_{Disloc} (kJ mol^{-1})	223	445	530	480
Activation volume for dislocation creep, V_{Disloc} (10^{-6} m^3/mol)	0	0	13	10
Pre-exponential constant for Peierls creep, log($B_{Peierls}$) (Pa^{-n} s^{-1})	-	-	11.76	-
Activation energy for Peierls creep, $E_{Peierls}$ (kJ mol^{-1})	-	-	540	-
Peierls stress, $\tau_{Peierls}$ (GPa)	-	-	8.5	-

[a]Dislocation creep parameters for upper crust: wet quartzite [*Gleason and Tullis*, 1995], lower crust: mafic Pikwitonei granulite [*Wilks and Carter*, 1990], strong mantle: dry olivine [*Hirth and Kohlstedt*, 2003], weak mantle: wet olivine, i.e., 500 ppm H/Si [*Hirth and Kohlstedt*, 2003] which is included in the pre-exponential factor. In diffusion creep parameters for strong mantle and weak mantle [*Hirth and Kohlstedt*, 2003], the grain size is held constant at 6 mm and is included in the pre-exponential factors. Peierls creep parameters for strong mantle [*Kameyama et al.*, 1999]. Weak mantle never reaches the required stress level of ≈500 MPa which is why we do not implement Peierls in the asthenospheric mantle.

[b]Linear decrease of μ from 0.6 to 0.06 between strain values of 0 and 1.

value α_{crit}, and $\sigma_V = 0$ otherwise. The exact value of α_{crit} depends on the Poisson ratio (for incompressible materials with $\nu = 0.5$, α_{crit} equals 71°, in more realistic cases where $\nu = 0.25$, α_{crit} equals 53°). Figure 2d depicts the differential stress evolution for all α. We find that $\sigma_1 - \sigma_3$ is indeed lower for pure extension than for strike-slip, as soon as the plastic limit is exceeded. The underlying reason are: (i) The largest principal stress σ_{H1} is a discontinuous function of α as it switches between the vertical σ_V and horizontal σ_{H2} at α_{crit}. (ii) Pure extension and low-obliquity deformation reach the yield limit at less displacement than strike-lip motion so that the differential stress remains at a lower level. This behavior is robust for all relevant parameter variations that are realized in the lithosphere (Table 1). Our results are thus in good agreement with long-known observations from fault mechanics.

[18] In order to allow analytic solution, a number of assumption such as simple elasto-plastic rheology, material homogeneity and zero gravity have to be made. With the following numerical solutions, we show that the characteristic dependency of the force on α is independent of these assumptions.

3. Modeling Approach

3.1. Experimental Setup

[19] In the numerical part of this study we can avoid the simplifications that where made for our analytic solutions. Namely, we apply realistic elasto-visco-plastic rheology with depth-dependent Drucker-Prager failure criterion to a layered Earth model under non-zero gravity.

[20] Our model consists of a rectangular segment of 750 km length, 250 km width and 150 km depth (Figure 3h) that includes a 20 km thick upper crustal layer of wet quartzite rheology [*Gleason and Tullis*, 1995], a lower crustal layer of 15 km thickness with mafic granulite properties [*Wilks and Carter*, 1990], and a 45 km thick layer of strong mantle material with dry olivine rheology [*Hirth and Kohlstedt*, 2003]. Taking into account the higher water content of the asthenosphere, we use rheological parameters of wet (i.e. 500 ppm H/Si) olivine in the lowermost layer below 80 km depth [*Hirth and Kohlstedt*, 2003]. All rheological parameters are listed in Table 1.

[21] A constant temperature is prescribed for the top and bottom surfaces of the model (0 °C and 1350 °C, respectively), while zero heat flow conditions are adopted for lateral boundaries. Numerical experiments are started with an equilibrium temperature distribution such that the 1350 °C isotherm is situated at 100 km depth, which accounts for thermal lithospheric thickness within mobile belts like the Damara Belt or the Pan-African Belt of Central Africa [*Artemieva*, 2006]. Moreover, a setting where the thermal lithosphere-asthenosphere boundary is located 20–30 km below the chemical lithosphere-asthenosphere boundary (here initially at 80 km) remains stable for several 100 Ma if small-scale convection is taken into account [*Sobolev et al.*, 2009]. The setup is applied to mobile belts since rifting often localizes along former plate sutures. A thicker chemical and thermal lithosphere that is encountered for rifts in undeformed continents will affect the magnitude of the involved tectonic forces but not the main outcome of this publication. After the first time step the thermal initial condition is relaxed and only the bottom temperature is prescribed. From that moment on, the thermal lithosphere-asthenosphere boundary results self-consistently from the combined effects of heat conduction and advection. The prospective rift zone is introduced in the thermal initial condition by a small temperature deviation along strike: the 1350 °C isotherm is elevated from 100 km to 80 km in a narrow zone of 20 km width (Figure 3). This setup essentially anticipates a small

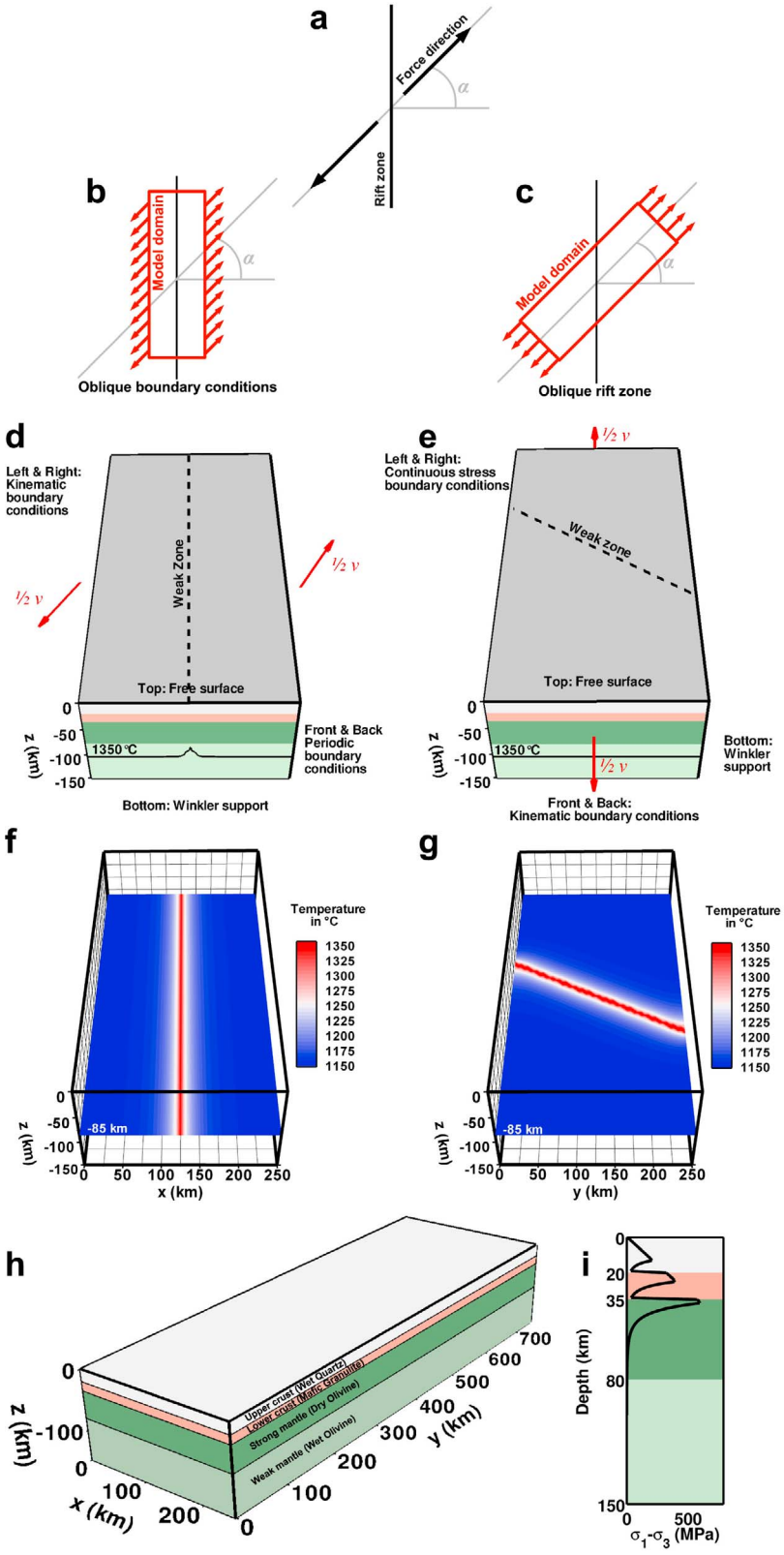

Figure 3. (a) Schematic view of oblique rifting where α designates the angle of obliquity. (b) General setup with oblique boundary conditions. (c) General setup with a rift zone that is oblique to the boundaries. (d, e) Boundary conditions for both setups. Extensional velocities are marked as red arrows. (f, g) Horizontal slice in 85 km depth depicting the initial thermal perturbation to localize rifting. (h) Rheological setup. (i) Yield strength profile (differential stress) for a strain rate of 1.3 10^{-15} s^{-1} that corresponds to the model description in Section 3.2.

amount of lithospheric necking which focuses the extensional deformation into the desired rift axis. This is one way of representing a weak zone. Alternative approaches are crustal thickening [*van Wijk*, 2005], implementation of a weak plastic seed [*Huismans and Beaumont*, 2003], or mechanical anisotropy [*Tommasi and Vauchez*, 2001]. Please note that all of these techniques will result in lithospheric necking comparable to our initial condition after a small amount of extension.

[22] As mentioned before, the locus and orientation of Earth's rift zones is controlled by the magnitude and direction of the plate-driving forces as well as by the location of inherited suture zones. In this study, we reduce complexity by considering a lithospheric segment of several hundred kilometers in width and length that is small compared to Earth's tectonic plates. Hence, tectonic forces that act on entire plates (ridge push, mantle drag) or plate boundaries (slab pull) will enter our model domain via the lateral boundaries. At any real rift zone, the direction of the extensional force will be constrained by the overall plate configuration. In order to investigate the role of rift obliquity, however, we vary the extensional direction between 0° and 90° with respect to the rift axis. In nature, the interaction between the obliquity-dependent rift force and the large scale plate forces will result in the overall plate kinematics.

[23] In this study, we model oblique extensional settings using two distinct kinds of models differing in the positioning of the model domain: (i) The model sides are parallel to the prospective rift zone while oblique boundary conditions are applied along strike. The front and back side are thereby connected via periodic boundary conditions (Figures 3b, 3d, and 3f). (ii) The initial weak zone is situated obliquely to the boundaries where face-perpendicular velocities are applied at the front and backside, whereby on the left and right boundary, continuous stress boundary conditions (described in next section) are implemented (Figures 3c, 3e, and 3g). The reason why two setups are chosen is of numerical nature: Prescribing the velocity distribution across a zone of deformation inhibits localization feedbacks and results in a zone of deformation which does not evolve self-consistently. We prescribe extensional velocities at the boundaries in x-direction which means that we have to avoid contact between a fault zone and these boundaries. By applying oblique boundary conditions the prospective rift zone lies parallel to the x-axis and the angle of obliquity can be varied freely between 0° (pure extension) and 90° (strike-slip). Within the oblique weak zone setup the location of the prospective rift zone varies with the angle of obliquity. Since the deformation zone is not allowed to touch the extending boundaries, the angle of obliquity is confined to a certain range. Thus, our geometry of 750 km length and 250 km width limits the rift angle to maximal 60°. Only one shear zone can be introduced for oblique boundary conditions, due to the periodic boundaries used in y-directions. Here lies the advantage of the oblique weak zone setup, where multiple rift zones with different angles of obliquity may be studied within the same model domain.

3.2. Numerical Modeling Techniques

[24] We use the implicit, Arbitrary Lagrangian-Eulerian (ALE), three-dimensional FEM code SLIM3D (Semi-Lagrangian Implicit Model for 3 Dimensions) [*Popov and Sobolev*, 2008] to solve the thermomechanically coupled conservation equations of momentum

$$-\frac{\partial p}{\partial x_i}+\frac{\partial \tau_{ij}}{\partial x_j}+\rho g_i=0 \tag{19}$$

energy

$$\rho C_p\frac{\mathrm{D}T}{\mathrm{D}t}-\frac{\partial}{\partial x_i}\left(\lambda\frac{\partial T}{\partial x_i}\right)-\tau_{ij}\dot{\varepsilon}_{ij}-\rho A=0 \tag{20}$$

and mass

$$\frac{1}{K}\frac{\mathrm{D}p}{\mathrm{D}t}-\alpha_T\frac{\mathrm{D}T}{\mathrm{D}t}+\frac{\partial v_i}{\partial x_i}=0 \tag{21}$$

with pressure p (defined as mean stress), coordinates x_i, time t, stress deviator τ_{ij}, density ρ, gravity vector g_i, heat capacity C_p, temperature T, material time derivative D/Dt, heat conductivity λ, strain rate deviator $\dot{\varepsilon}_{ij}$, radioactive heat production A, bulk modulus K, thermal expansivity α_T, and velocities v_i. Parameter values are given in Table 1. The Einstein summation rule applies for repeated indices.

[25] The Lagrangian formulation is used to solve the system of equations for the primary variables, namely incremental displacement (Δu), and temperature (T) using the Galerkin procedure of the Finite Element Method. Remeshing is used to prevent large grid distortion and to track motion of the free surface. During the remeshing phase we use the marker-in-cell technique to resolve the advection of the material phases and history variables, such as Cauchy stress and accumulated plastic strain.

[26] The conservation equations are solved with simultaneous consideration of the constitutive laws that relate deformation and stress. An elasto-visco-plastic rheology is implemented adopting additive decomposition of the deviatoric strain rate into elastic, viscous, and plastic components [*Simo and Hughes*, 2000].

$$\dot{\varepsilon}_{ij}=\dot{\varepsilon}_{ij}^{el}+\dot{\varepsilon}_{ij}^{vs}+\dot{\varepsilon}_{ij}^{pl}=\frac{1}{2G}\hat{\tau}_{ij}+\frac{1}{2\eta_{eff}}\tau_{ij}+\dot{\gamma}\frac{\partial Q}{\partial \tau_{ij}} \tag{22}$$

[27] Where G is the elastic shear modulus, $\hat{\tau}_{ij}$ the objective stress rate, η_{eff} the effective creep viscosity, $\dot{\gamma}$ the plastic multiplier, and Q is the plastic potential function.

[28] Following the approach of *Kameyama et al.* [1999], we use three types of creep mechanisms: diffusion, dislocation, and Peierls:

$$\eta_{eff}=\frac{1}{2}\tau_{II}\left(\dot{\varepsilon}_{Diff}+\dot{\varepsilon}_{Disloc}+\dot{\varepsilon}_{Peierls}\right)^{-1} \tag{23}$$

with τ_{II} being the second invariant of deviatoric stress and $\dot{\varepsilon}_{Diff}$, $\dot{\varepsilon}_{Disloc}$, as well as $\dot{\varepsilon}_{Peierls}$ the second invariant of strain rate for the respective creep mechanism. The latter are computed as follows:

[29] Diffusion creep

$$\dot{\varepsilon}_{Diff}=B_{Diff}\tau_{II}\exp\left(-\frac{E_{Diff}+pV_{Diff}}{RT}\right) \tag{24}$$

[30] Dislocation creep

$$\dot{\varepsilon}_{Disloc} = B_{Disloc}(\tau_{II})^n \exp\left(-\frac{E_{Disloc} + pV_{Disloc}}{RT}\right) \quad (25)$$

[31] Peierls creep

$$\dot{\varepsilon}_{Peierls} = B_{Peierls}\left(\frac{\tau_{II}}{\beta\tau_{Peierls}}\right)^s \exp\left[\frac{-E_{Peierls}}{RT}(1-\beta)^2\right] \quad (26)$$

where

$$s = 2\beta(1-\beta)\frac{E_{Peierls}}{RT} \quad (27)$$

[32] In the above equations B_{Diff}, B_{Disloc}, $B_{Peierls}$ and E_{Diff}, E_{Disloc}, $E_{Peierls}$ denote the creep parameter and activation enthalpy, respectively, of each correspondent mechanism. R is the gas constant, n the power law exponent, $\tau_{Peierls}$ the Peierls stress, and $0 < \beta < 1$ is an adjustable approximation parameter [see *Popov and Sobolev*, 2008, and references therein].

[33] Brittle deformation is implemented by means of the standard Mohr-Coulomb plasticity model:

$$f = \frac{1}{2}(\sigma_{\max} - \sigma_{\min}) + \frac{1}{2}(\sigma_{\max} + \sigma_{\min})\sin\varphi - c\cos\varphi \le 0 \quad (28)$$

where f defines the yield surface, $\sigma_{\max}$ and $\sigma_{\min}$ are maximum and minimum principal stresses, φ is the friction angle, and c cohesion. During every computational step, a viscoelastic trial stress is calculated assuming constant viscosity. If the trial stress locates beyond the yield surface, plastic failure takes place. In this case, the stress point is projected onto the yield surface under application of the Prandtl-Reuss flow rule and plastic strain is increased accordingly.

[34] Several weakening mechanisms exist in the model that tend to localize deformation in the lithosphere:

[35] 1. The ongoing shear deformation within a fault zone leads to a reduction of crustal fault strength [*Zoback et al.*, 1987; *Provost and Houston*, 2003]. This process is strongly influenced by the presence of fluids within the crust that are required to generate weak fault rocks. Fluids can not easily advance into the mantle which is why we apply friction softening only in the crust. The process itself is approximated here using a plastic strain-dependent friction angle. In our experiments, the friction angle decreases linearly by 90 % of the initial value when plastic strain reaches 1, and remains constant for larger strains.

[36] 2. Another inherent weakening mechanism is shear heating that is proportional to $\tau_{II}\dot{\varepsilon}_{II}$ (equation (20)): Large strain rates lead to increased temperature which lowers the effective viscosity. A smaller viscosity attracts deformation and thus increases the strain rate.

[37] 3. Dislocation creep features a power law dependency between strain rate and stress. For constant strain rate, this causes a decreasing viscosity if stresses increase (i.e. stress softening). On the other hand, if stress is assumed constant, the power law dependency results in lower viscosity for an increase in strain rate (i.e. strain rate softening).

[38] The extensional setting is represented here using appropriate Dirichlet boundary conditions prescribing the velocities over the entire sides. Unless otherwise indicated, the extension velocities in this publication refer to full spreading rates, so that extension of 10 mm/yr is applied by prescribing boundary velocities of 5 mm/yr at each side. Mechanical boundary conditions for upper and lower faces consist of a free surface at the top and Winkler support at the bottom. The lower boundary moves upward during extension, however during each remeshing it is reset to 150 km while new asthenospheric markers are introduced. The straightforward implementation of these boundary conditions constitutes a major advantage of the deformable mesh within the Finite Element framework. Two additional implementations can be used for lateral boundaries: (i) In the oblique boundary condition setup, periodic boundaries equalize all variables at one side of the model to the opposite boundary. The periodicity resembles that of a circle, however in Cartesian coordinates. (ii) The continuous stress boundary conditions used in the oblique weak zone setup constitute an extension of the free slip boundary. While volumetric stresses for the free slip formulation do not change across the boundary, shear stresses are assumed to be zero. The analogon of free-slip boundaries in nature would be very weak, vertical faults that cut through the whole lithosphere. By assuming that both volumetric and face-parallel shear components of the stress tensor remain identical across the boundary, we extend the free slip boundary condition. Note that velocities that are perpendicular to the boundary remain zero like for the free-slip condition.

[39] We use cubic finite elements with 8 displacement nodes and volume-averaged derivatives of the shape function. The closest mixed-finite element discretization would be Q1P0. An ad-hoc stabilization of pressure oscillations is implemented [*Popov and Sobolev*, 2008]. Unless otherwise indicated, elements have 5 km edge length resulting in 225000 elements within the domain. The implicit time stepping allows for a step size of 20 ky so that 500 steps suffice to compute 10 My evolution. The current version of SLIM3D solves the discretized conservation equations using the direct parallel shared memory solver PARDISO [*Schenk and Gärtner*, 2004].

4. Results

4.1. Oblique Boundary Conditions

[40] First, we focus on the setup with oblique boundary condition (Figures 3b, 3d, and 3f). In the following, we study three distinct cases with angle of obliquity $\alpha = 0°$, $60°$, $90°$, corresponding to pure extension, high obliquity, and strike-slip deformation, respectively (Figure 4; corresponding animations can be found in the auxiliary material).[1]

[41] All models exhibit strain localization at the center of the computational domain above the prescribed thermal perturbation. However, the models differ significantly with respect to shear zone geometry, evolution of lithospheric thinning and mechanical strength of the domain.

[42] During pure extension ($\alpha = 0°$), the uppermost mantle and crust undergo necking (Figures 4a and 4b). Below the rift center, lithospheric material is replaced by hot advective upwelling. Cooling of this upwelling takes place much

[1] Auxiliary materials are available in the HTML. doi:10.1029/2011JB008860.

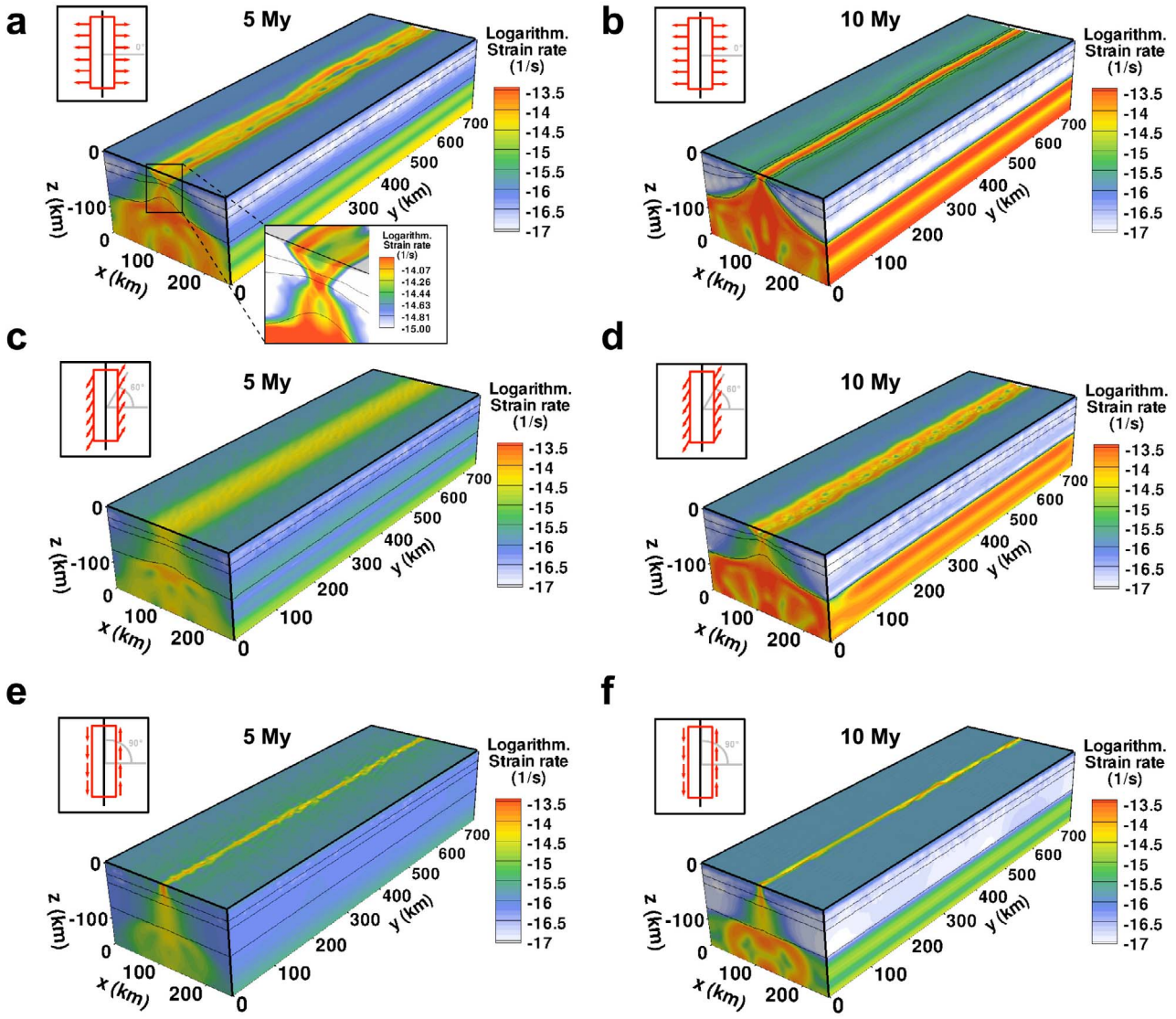

Figure 4. Oblique boundary conditions. Shown is the second invariant of strain rate $\dot{\varepsilon}_{II}$ at 5 My and 10 My. Black lines designate phase boundaries between upper and lower crust as well as strong and weak mantle. (a, b) Pure extension ($\alpha = 0°$). (c, d) High obliquity ($\alpha = 60°$). (e, f) Strike-slip deformation ($\alpha = 90°$). Corresponding animations can be found in the supplementary material.

slower than its intrusion leading to a loss of strength in the center of the domain. A set of shear zones evolves in the rift zone of which two large normal faults cut through the crust. After roughly 10 My, mantle material reaches the surface which finalizes break-up and initiates seafloor spreading. The small along-strike variations that occur during the highly non-linear localization process are due to numerical noise that derives from a random marker distribution.

[43] The highest possible angle of obliquity ($\alpha = 90°$) results in strike-slip deformation of the domain (Figures 4e and 4f). Neither crustal nor lithospheric necking takes place, because the boundary velocity contains no rift-perpendicular extensional component. One large strike-slip zone emerges shortly after the model start that is underlain by a broad zone of deformation in the viscous domain. Due to the intrinsic weakening mechanisms, the frictional resistance decreases with ongoing strain which attracts further deformation. After 10 My the mature system focuses most strain into the strike-slip zone.

[44] Oblique rifting features many characteristics of both pure extension and strike-slip deformation (Figures 4c and 4d). In the oblique models, the zone of deformation is much more diffuse than in the end-member cases 0° and 90°, until it localizes into distinct shear zones that strike at a certain angle to the boundary velocity, comparable to en-echelon faulting. This behavior has also been observed in many analog models [*Corti et al.*, 2003; *Agostini et al.*, 2009; *Autin et al.*, 2010] and in some numerical experiments [*van Wijk*, 2005; *Popov and Sobolev*, 2008]. The angle of the individual shear zones with respect to the model boundaries reflects the direction of the principal stress directions as discussed in *Withjack and Jamison* [1986].

[45] The general structure of the models does not vary significantly along strike, and remains identical if the model length in that direction is varied. Note that periodic boundary conditions along strike avoid any otherwise occurring boundary effects. Moreover, the temporal history of mechanical variables is not influenced, if the model domain in y-direction is reduced to the size of one element. Although the domain is in this case essentially two-dimensional, the velocities still bear three components, which results in a model that we use to call 2.5-dimensional [*Sobolev et al.*, 2005]. A major advantage of the domain shortening is that much less computational effort is necessary if elements keep their size of 5 km. Alternatively, we have the opportunity to increase the resolution significantly at comparable computation times. Below we use element sizes of 1 km.

[46] In the above models, we apply a constant velocity at the lateral boundaries. Keeping the velocity constant requires a specific boundary force F that can be computed from stress components σ_{ij} at the boundary. For that purpose, we first compute the integrated stress tensor S_{ij}:

$$S_{ij} = \frac{1}{L_y L_z} \int\int \sigma_{ij} \; dydz \tag{29}$$

where the length of the model domain in y and z direction are denoted L_y and L_z, respectively. The full boundary force F_{full} results from the Pythagorean addition of those stress components S_{ij} that locate on the face of the box with normal in x-direction (S_{xx}, S_{xy}, and S_{xz}):

$$F_{full} = \sqrt{S_{xx}^2 + S_{xy}^2 + S_{xz}^2} \cdot L_z \tag{30}$$

[47] If the extensional velocity was zero, the horizontal stress S_{xx} would be equal to the non-zero, lithostatic stress S_{zz}, while S_{xy} and S_{xz} would vanish [*Turcotte and Schubert*, 2002]. This means that F_{full} is not appropriate to measure the tectonic force since it is non-zero although no deformation takes place. In order to calculate the correct tectonic force we introduce the tectonic stress ΔS [*Artyushkov*, 1973]: Applied boundary velocities increase S_{xx} by ΔS so that $S_{xx} = S_{zz} + \Delta S$, whereas the shear components S_{xy} and S_{xz} remain unchanged. In the following, we compute the tectonic force F due to the tectonic stress contribution:

$$\begin{aligned} F &= \sqrt{(\Delta S)^2 + S_{xy}^2 + S_{xz}^2} \cdot L_z \\ &= \sqrt{(S_{xx} - S_{zz})^2 + S_{xy}^2 + S_{xz}^2} \cdot L_z. \end{aligned} \tag{31}$$

[48] That formula is the three-dimensional analog of the commonly used two-dimensional definition of the tectonic extensional force [e.g., *Bialas et al.* 2010].

[49] F reflects the integrated material strength and thus strongly depends on the internal thermomechanical structure of the model. As we showed in the previous paragraph, this structure is decisively influenced by the direction of the boundary velocity. In a set of experiments, we evaluate the boundary force for a constant boundary velocity of 10 mm/yr (full extension rate) whose direction varied between $\alpha = 0^\circ$ (pure extension) and $\alpha = 90^\circ$ (strike-slip) (Figure 5a). First, we consider the regime of pure extension (red curve): Within the first time steps, stresses are propagated elastically, and the force grows linear with time, until yield strength is reached at 13 TN/m. Due to lithospheric necking, the strength of the lithosphere decreases with time to 1.5 TN/m at around 10 My, where mantle material reaches the surface and break-up is completed. In the case of strike-slip deformation (blue curve in Figure 5a), following the period of elastic stress propagation, yield strength is reached at 7 TN/m. Due to the lack of lithospheric necking, the force decreases much slower than for the case of pure extension until it reaches 4 TN/m at 10 My. The weakening is caused solely by shear heating and strain softening, which will be investigated later on. Oblique rifting ($10^\circ \leq \alpha \leq 80^\circ$) constitutes a mixture of both end-member cases. Especially the maximum force varies smoothly, although nonlinear with the rift angle.

[50] The absolute value of the extensional velocities can be expected to have distinct control on the tectonic force. We investigate that issue by varying the extensional velocity by a factor of 2 and 0.5. Correspondingly, we use different calculation times (5 My and 20 My) so that the absolute extension remains identical. For simplicity, we investigate only the cases where α equals 0° and 90° (Figure 5b). Two primary effects can be observed: (i) Since higher velocities (20 mm/yr) imply higher strain rates, the viscous domains exhibit higher stress values and the integrated lithospheric strength is elevated. This explains why the maximum force increases when faster extension is applied. The opposite is true for low velocities of 5 mm/yr. (ii) Thermal equilibration of the lithosphere counteracts the weakening effect of lithospheric necking. If extensional rates are small, there is more time for conductive lithospheric cooling which is why the effective strength of the lithosphere decreases more slowly [e.g., *Kusznir and Park*, 1987]. This effect is relevant only for slow extension (5 mm/yr) illustrated by the fact that here the force at 20 My is distinctly larger than the final force for both the 10 mm/yr and 20 mm/yr experiments.

[51] The maximum force value is measured at the yield limit before any weakening mechanisms play a role. This value can be compared directly to the yield force computed in the analytical solution of section 2. Figure 5c displays the dependence of yield force F on the angle of obliquity α. Despite the severe assumptions of the analytical approach, the correspondence between the analytical curve (with $\nu = 0.23$ and $L_z = 47$ km) and the numerical results is very good, ensuring the robustness of our results.

[52] The temporal behavior of the force in Figure 5a is dominated by diverse weakening effects like lithospheric necking, crustal strain-dependent friction softening, shear heating, and power law rheology in the viscous domain. We study the effect of friction softening and shear heating by successively switching these effects on or off (Figure 6). Lithospheric necking and Non-Newtonian dislocation creep, however, are so strongly inherent that it is not feasible to disable them. Both strain softening and shear heating become effective only after a few My, when either deformation or strain rate is high enough. In the case of pure extension, lithospheric necking is the major weakening mechanism, although it is enhanced by shear heating and friction softening. After 9 My when break-up is complete, stresses and crustal deformation in the rift center become very small so that the force becomes independent of friction softening and shear heating. In the strike-slip setting, no

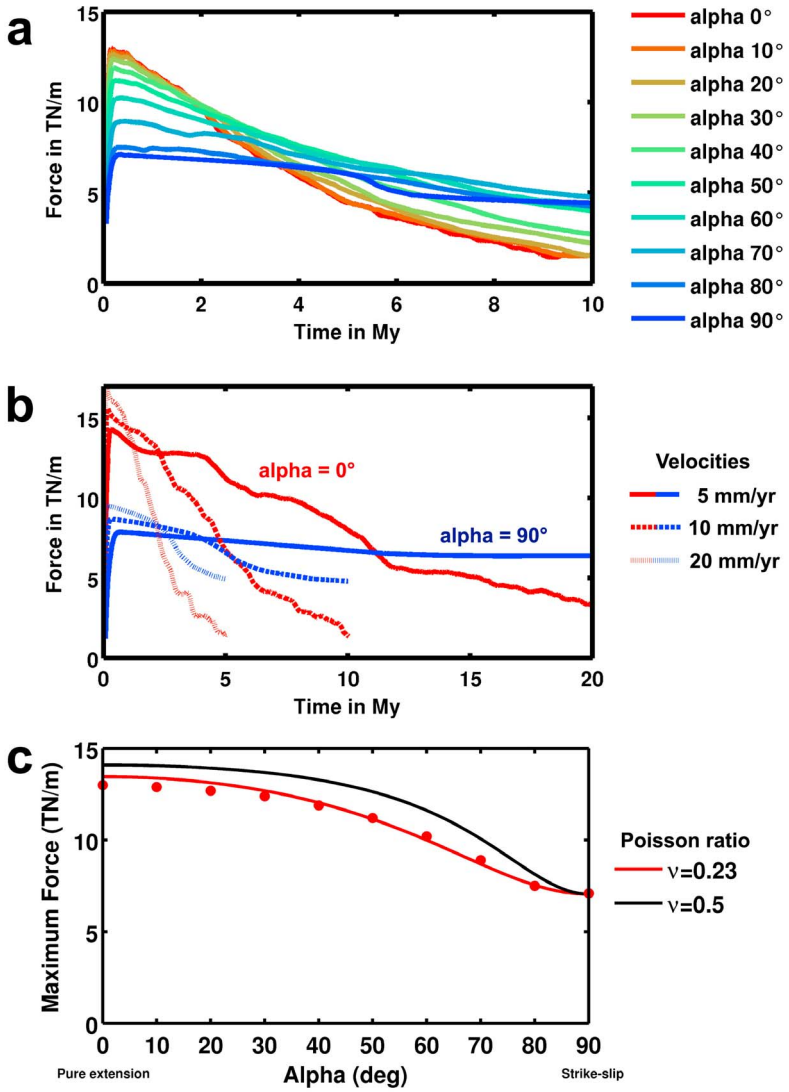

Figure 5. Tectonic force evolution in numerical experiments. (a) The required force to maintain extensional velocities. (b) Influence of extension velocity. (c) Comparison between maximum force values of numerical experiments (red dots) and analytic calculations for volume-conserving (ν = 0.5, blue curve) and realistic (ν = 0.23, red curve) values of the Poisson ratio. The layer thickness for the analytical solutions is L_z = 47 km.)

upwelling takes place and weakening is controlled by shear heating and friction softening. If both mechanism are switched off, the force remains constant or even increases slightly due to lithosphere cooling. For this setup and the applied parameterizations, we find that friction softening is more important than shear heating and the influence of both effects is responsible for about 2 to 3 TN/m force reduction.

4.2. Oblique Rift Zone

[53] If oblique rifting requires less force, what happens if two prospective rift zones of different obliquity compete in the same tectonic setting? In this section, we address that question using an alternative setup to oblique boundary conditions by implementing a rift zone that is oblique to the boundaries (Figures 3c, 3e, and 3g). We first display the evolution of an oblique and a perpendicular rift zone before we investigate a setting with both rifts simultaneously. Again, we use a small temperature perturbation at the bottom of the lithosphere to prescribe the orientation of a prospective rift zone. This perturbation has the same height, width and average cross section as in the previous setting. While the rift zone is oblique, the boundary velocities are now perpendicular to the sides of the domain. We apply extension at the front and back of the model, while the lateral sides feature continuous stress boundary conditions. As in the previous setup, we look at rift angles $\alpha = 0°$ and 60°. The case of $\alpha = 90°$ can not be implemented for this setting, as this would mean to prescribe velocities within the shear zone which inhibits the natural localization process.

[54] Pure extension ($\alpha = 0°$) results in the formation of two finite-width normal faults, lithospheric and crustal necking (Figures 7a and 7b), just as in the setting of oblique boundary conditions. Oblique rifting ($\alpha = 60°$) again shows distinct shear zones that cut through the rift zone, striking

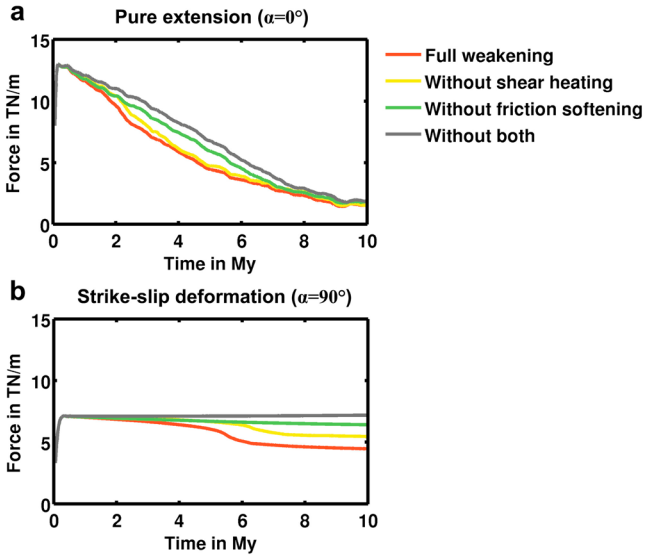

Figure 6. Influence of weakening processes: Shear heating $(\sim\tau_{II}\dot{\varepsilon}_{II})$ and friction softening $(\sim\varepsilon_{II})$. Please refer to the text for more details on the weakening mechanisms. (a) Weakening for pure extension is dominated by lithosphere necking. (b) The strike slip setting is controlled by shear heating and friction softening.

subparallel to the weak zone (Figures 7c and 7d). However, some discrepancies to Figure 4 are visible. The boundaries somewhat affect the form of the rift so that the endings of the shear zone are slightly bent. Furthermore, as the model length in extensional direction is larger in the present setting, but spreading velocities remained identical, the mean strain rate in the present setup is smaller than that of the previous section. Nevertheless, as soon as deformation is localized into the rift zone of approximately the same width, rift-relevant strain rates become effectively identical to the setup with oblique boundary conditions which is why the general dynamics of both setups is very similar. These differences have only minor effects on the temporal evolution of the required boundary force. The maximum forces for the oblique boundary setting and the oblique weak zone setup are the same; only the timing is slightly different, due to different strain rates.

[55] Finally, we introduce two prospective rift zones of distinct orientation ($\alpha_1 = 0°$ and $\alpha_2 = 60°$) into the model (Figures 7e and 7f), while all other parameters and boundary conditions remain the same. Essentially, both setups of Figures 7a and 7b and Figures 7c and 7d are appended in a row, whereby the length of the computational domain is increased to 900 km. During the first several million years, both weak zones are simultaneously active, while the strain rate of the oblique rift grows steadily at the expense of the perpendicular zone. The oblique rift zone attracts successively more strain until the boundary-perpendicular zone of deformation becomes extinct at roughly 8 My. This result is independent of the specific implementation. Variations in width and height of the initial temperature heterogeneity, the extensional velocity or the size of the model domain did not change the overall behavior. Moreover, the outcome can be related to *Chemenda et al.* [2002] who showed that in analog models of extending, homogeneous lithosphere faults develop preferentially at an angle of ≈60° toward the extensional direction. Although our lithosphere is not homogeneous, and the boundary conditions differ, both experiments show that rift obliquity is mechanically preferred.

4.3. Dynamic Boundary Conditions

[56] Interaction between a rift zone and the forces that drive plate motion can be of two distinct kinds: Either dynamics of the rift zone influence the overall force balance, or they do not. Velocity boundary conditions are best applicable in the latter case when the integrated strength of the rift zone is small compared to the plate-driving forces. In this case, the extensional velocity of the rift will depend only on the large-scale force balance and plate geometries. If the rift's strength, however, is comparable to the plate-driving forces, it will feed back on the extensional velocities. This is the case for the opening of large oceanic basin, where the length of the rift zones exceeds several 1000 kilometers.

[57] In the previous sections, we held the boundary velocities constant and computed the required force. Here, we reverse that approach and prescribe the boundary force and its direction in order to compute resulting velocities. We showed beforehand that oblique rifting is mechanically preferred, however higher obliquity results in less rift-perpendicular extension. Strike-slip motion for instance may require least force, but it does not result in break-up since the plates do not separate. In this section we investigate whether an optimal extensional angle exists that maximizes rift-perpendicular extension for a given boundary force.

[58] Under the application of a constant force to any brittle material, three dynamic regimes can be anticipated: (i) If forces are too low they can not induce plastic failure so that deformation stops according to the purely elastic response. (ii) The applied force overcomes the plastic yields strength. The system deforms according to its internal structure resulting in boundary velocities that can be regarded as an integrated response to the external load. (iii) Weakening processes like lithospheric necking dominate the mechanical behavior. The decreasing strength of a maturing rift is compensated by rising velocities in order to fulfill the constant force boundary condition. Increasing velocities lead to even more weakening and a runaway process is induced. Rift zones bear a certain strength, while mid-oceanic ridges are extremely weak. During the transition between rifting and seafloor spreading, the runaway process stops when the extensional velocity becomes independent of lithospheric strength and finally reflects the interplay of plate boundary forces and mantle drag. We address this issue in our model by implementing an upper limit to velocities of 50 mm/yr that agrees well with typical values for ocean floor spreading rates in the Atlantic [*Müller et al.*, 2008]. Once this velocity limit is reached, constant velocity boundary conditions are used like in the previous subsections. These mixed force-velocity boundary conditions allow to model the whole process from rifting to break-up until seafloor spreading is initiated and they reproduce the observed rift velocities of 5 to 20 mm/yr [*Buck*, 1991] together with typical seafloor spreading rates in the order of 40 to 100 mm/yr [*Müller et al.*, 2008].

[59] Using the same setting of oblique boundary conditions as in section 3.1, we apply forces of 8 TN/m and 11 TN/m that are high enough to induce plastic failure for

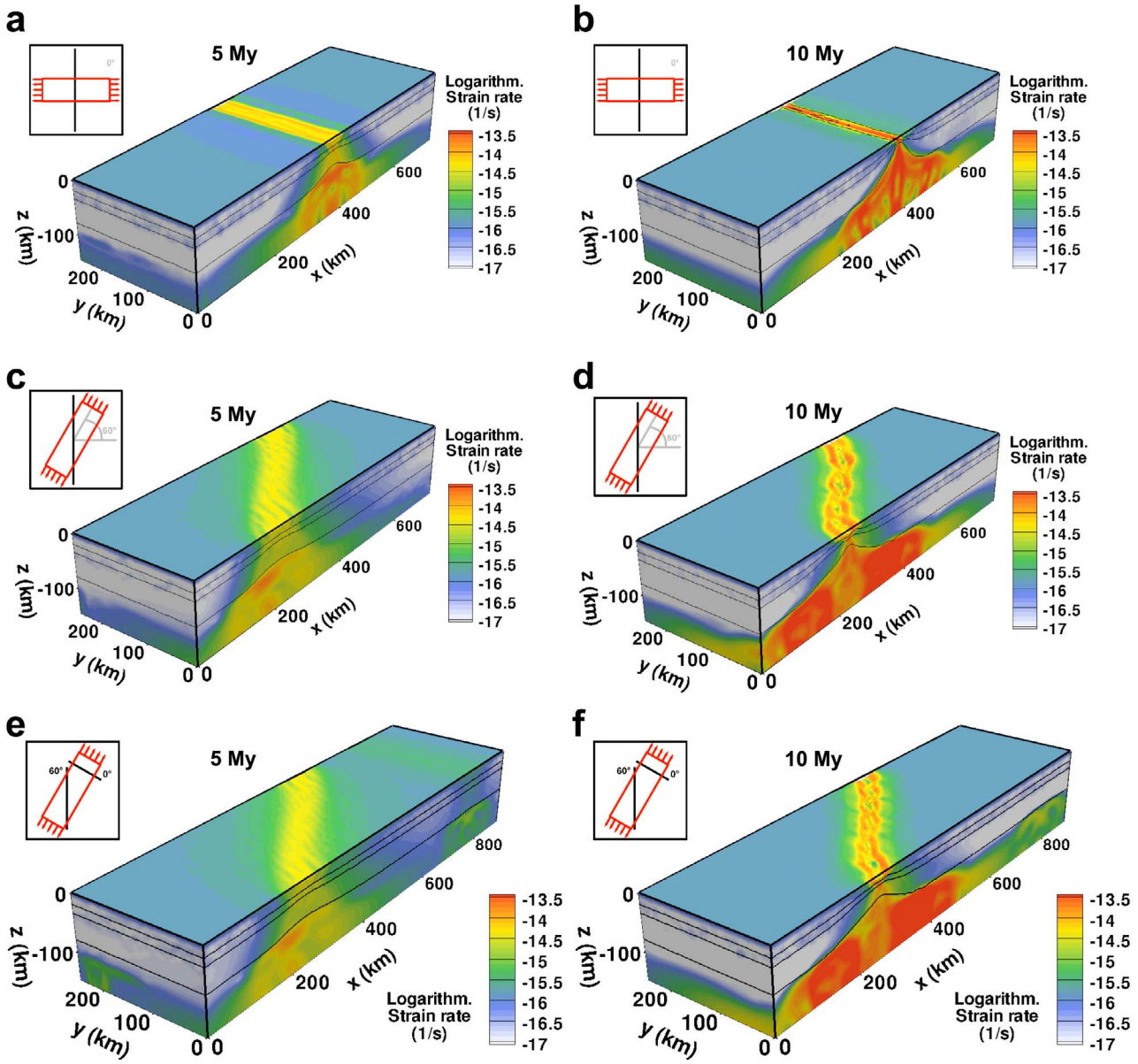

Figure 7. Oblique weak zones. Shown is the second invariant of strain rate at 5 My and 10 My. Black lines designate phase boundaries between upper and lower crust as well as strong and weak mantle. (a, b) Pure extension ($\alpha = 0°$). (c, d) High obliquity ($\alpha = 60°$). (e, f) Simultaneous deformation of extension-perpendicular ($\alpha = 0°$) and highly oblique weak zones ($\alpha = 60°$). Corresponding animations can be found in the supplementary material.

the prescribed initial lithospheric structure (Figure 8). Again, we consider distinct rift angles that vary between 0° (pure extension) and 90° (strike-slip deformation), while all other parameters are identical to those of section 3.1. Note that in Figure 5 the maximum force (13 TN/m) for a constant velocity of 10 mm/yr has been higher than the values in this experiment. The model that is most influenced by the force limit is that of pure extension (red curves in Figures 8a, 8c, and 8e). This follows from our previous result that pure extension requires the largest force to deform at constant strain. Its velocity remains at low levels below 5 mm/yr during the first 3 My. Only then lithospheric necking weakens the rift zone sufficiently so that velocities increase quickly up to 50 mm/yr within 1 My. Once the limiting velocity of 50 mm/yr is reached and hence break-up occurred, the force decreases below 2 TN/m. The oblique models result in similar behavior except that the limiting velocity is reached more quickly. The strike-slip end-member (blue line) even commences with 50 mm/yr, as is does not require 11 TN/m to reach the velocity limit. Nevertheless, all deformation is concentrated on the strike-slip zone so that no rifting and no break-up takes place. For the intermediate settings ($10^{\circ} \leq \alpha \leq 80^{\circ}$) rift-perpendicular extension does occur and deformation evolves faster than for the rift-perpendicular extension. The largest rift-perpendicular extension during the first 5 My can be observed for rift

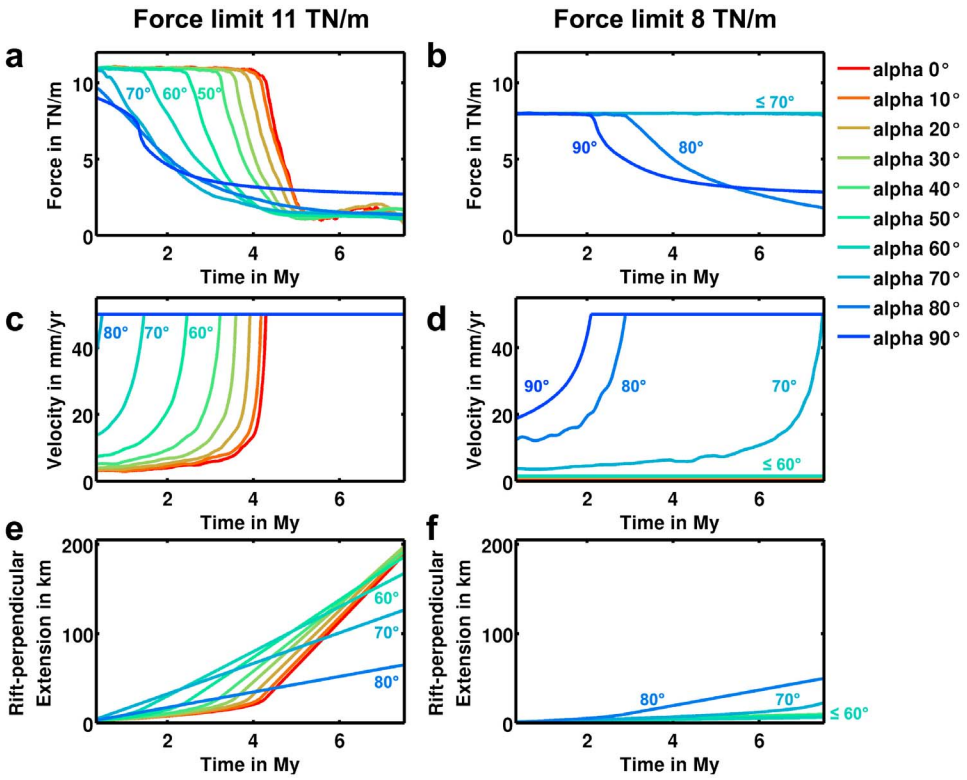

Figure 8. Dynamic boundary conditions: Boundary velocities are adjusted so that a maximum force of (a, c, e) 13 TN/m and (b, d, f) 8 TN/m is not exceeded. If forces fall below that threshold, velocities are fixed to 50 mm/yr (see text for further explanations).

angles of 60° and70° (Figure 8e); while $\alpha = 0°$ yields 20 km rift-perpendicular extension at 5 My, $\alpha = 60°$ results in 100 km. If force is lower, say 8 TN/m, only highly oblique rifts are developing (Figures 8b, 8d, and 8f) while settings with $\alpha \leq 60^{\circ}$ do not exceed velocities of 1.5 mm/yr. In this case the largest extension (30 km) after 5 My is achieved for rifting with an obliquity of 80°. At forces below the lithospheric strength for the pure strike-slip (7 TN/m, see Figure 5) no rifting takes place for the considered lithospheric structure.

[60] This result implies that the optimal rift angle which maximizes rift-perpendicular extension decreases with time. We suggest that in the beginning of an oblique break-up process almost pure strike-slip faults tend to develop, like it is happening now at the Dead Sea Transform plate boundary. Later, less oblique faults may emerge and first break-up will likely take place at high-obliquity faults with α between 50° and 80°. Note that this hypothesis is best applicable if magmatic processes can be neglected, i.e. for non-volcanic rifts or during non-magmatic rift stages. If considerable amounts of melt are produced, dikes will intrude perpendicular to the principal direction of extension. This process decreases the required tectonic force for rift-perpendicular extension [*Buck*, 2007] and may strongly affect the dynamic evolution of the system. In nature, rifts are not free to evolve and this development interferes with the overall plate configuration. We therefore suggest to test whether this development can be observed in future kinematic reconstructions of break-up processes.

[61] Estimations of the continental lithospheric strength based on yield strength profiles show that the strength of continental lithosphere considerably exceeds the available tectonic forces [*Buck*, 2007]. The formulation of that problem is disputed since the apparent paradox resolves, when very low friction coefficients are used in the entire lithosphere [*Huismans and Beaumont*, 2003] or when additional mechanisms leading either to the weakening of the lithosphere (e.g., via Peierls creep [*Kameyama et al.*, 1999]), or to an increase in the effective extensional force are taken into account. Here we show that the tectonic force that is required to induce rifting depends on the angle of obliquity. Hence, a rift with zero obliquity may not be activated for a given tectonic force while an oblique rift generates sufficient extensional strain to result in continental break-up. If available tectonic forces are lower than pure strike-slip lithospheric strength no rifting takes place. In that case, continental break-up can only occur if the lithosphere experiences additional weakening either due to significant input of melts via diking [*Buck*, 2004] or interaction with a thermo-chemical plume [*Sobolev et al.*, 2011].

5. Conclusions

[62] Oblique extension facilitates the rift process. The major reason is that oblique motion requires less force in order to reach the plastic limit. Under idealized elasto-plastic conditions we analytically computed the necessary force to induce plastic behavior. It is approximately two times less for the strike-slip case if compared to pure extension. This result

is not in contradiction with classical fault mechanics since the observation that strike-slip motion requires more differential stress than pure extension can be reproduced by our calculations. The analytical computations agree very well with the numerical results derived from an elasto-visco-plastic model of a layered Earth segment. An important aspect of these findings becomes apparent if two rifts of identical properties compete in a non-magmatic setting whereby one rift is perpendicular and one oblique to the direction of extension: Our experiments show that the oblique rift zone will accommodate successively more extensional strain while deformation in the second rift stagnates. In force-limited settings, our modeling demonstrates that with realistic tectonic forces of less than 10 TN/m and a typical lithospheric thickness of about 100 km as encountered in mobile belts, oblique rifting is mechanically preferred. We suggest that rifts are most effective in accumulating rift-perpendicular extension if they start at high angles of obliquity and rotate to lower angles during rift maturation.

[63] **Acknowledgments.** This research is a product of SAMPLE (South Atlantic Margin Processes and Links with onshore Evolution), Priority Program 1375, funded by the German Research Foundation (DFG). We would like to thank Susanne Buiter and an anonymous reviewer for their detailed and productive comments that lead to significant improvements of the manuscript.

References

Agostini, A., G. Corti, A. Zeoli, and G. Mulugeta (2009), Evolution, pattern, and partitioning of deformation during oblique continental rifting: Inferences from lithospheric-scale centrifuge models, *Geochem. Geophys. Geosyst.*, *10*, Q11015, doi:10.1029/2009GC002676.

Allken, V., R. S. Huismans, and C. Thieulot (2011), Three-dimensional numerical modeling of upper crustal extensional systems, *J. Geophys. Res.*, *116*, B10409, doi:10.1029/2011JB008319.

Artemieva, I. M., (2006), Global 1° × 1° thermal model TC1 for the continental lithosphere: Implications for lithosphere secular evolution, *Tectonophysics*, *416*, 245–277.

Artyushkov, E. V. (1973), Stresses in the lithosphere caused by crustal thickness inhomogeneities, *J. Geophys. Res.*, *78*, 7675–7708, doi:10.1029/JB078i032p07675.

Autin, J., N. Bellahsen, L. Husson, M. Beslier, S. Leroy, and E. d'Acremont (2010), Analog models of oblique rifting in a cold lithosphere, *Tectonics*, *29*, TC6016, doi:10.1029/2010TC002671.

Bellahsen, N., C. Faccenna, F. Funiciello, J. Daniel, and L. Jolivet (2003), Why did Arabia separate from Africa? Insights from 3-D laboratory experiments, *Earth Planet. Sci. Lett.*, *216*, 365–381.

Bialas, R. W., W. R. Buck, and R. Qin, (2010), How much magma is required to rift a continent?, *Earth Planet. Sci. Lett.*, *292*, 68–78.

Braun, J., and C. Beaumont, (1989), A physical explanation of the relation between flank uplifts and the breakup unconformity at rifted continental margins, *Geology*, *17*, 760–764.

Buck, W. R. (1991), Modes of continental lithospheric extension, *J. Geophys. Res.*, *96*, 20,161–20,178, doi:10.1029/91JB01485.

Buck, W. R. (2004), Consequences of asthenospheric variability on continental rifting, in *Rheology and Deformation of the Lithosphere at Continental Margins*, edited by G. D. Karner et al., pp. 1–30, Columbia Univ. Press, New York.

Buck, W. R. (2007), Dynamic processes in extensional and compressional settings - the dynamics of continental breakup and extension, in *Treatise on Geophysics*, vol, 6, *Crust and Lithosphere Dynamics*, edited by A. B. Watts, pp. 335–376, Elsevier, New York.

Chemenda, A., J. Déverchère, and E. Calais (2002), Three-dimensional laboratory modelling of rifting: application to the Baikal Rift, Russia, *Tectonophysics*, *356*, 253–273.

Clifton, A. E., R. W. Schlische, M. O. Withjack, and R. V. Ackermann (2000), Influence of rift obliquity on fault-population systematics: results of experimental clay models, *J. Struct. Geol.*, *22*, 1491–1509.

Corti, G. (2008), Control of rift obliquity on the evolution and segmentation of the main Ethiopian rift, *Nat. Geosci. 1*, 258–262.

Corti, G., M. Bonini, S. Conticelli, F. Innocenti, P. Manetti, and D. Sokoutis (2003), Analogue modelling of continental extension: A review focused on the relations between the patterns of deformation and the presence of magma, *Earth Sci. Rev.*, *63*, 169–247.

de Wit, M. J. (2003), Madagascar: Heads it's a continent, tails it's an island, *Annu. Rev. Earth Planet. Sci.*, *31*, 213–248.

Edwards, R. A., R. B. Whitmarsh, and R. A. Scrutton (1997), The crustal structure across the transform continental margin off Ghana, eastern equatorial Atlantic, *J. Geophys. Res.*, *102*, 747–772, doi:10.1029/96JB02098.

Engen, Ø., J. I. Faleide, and T. K. Dyreng (2008), Opening of the Fram Strait gateway: A review of plate tectonic constraints, *Tectonophysics*, *450*, 51–69.

Gaina, C., R. D. Müller, B. Brown, T. Ishihara, and S. Ivanov, (2007), Breakup and early seafloor spreading between India and Antarctica, *Geophys. J. Int.*, *170*, 151–169.

Gleason, G. C., and J. Tullis, J. (1995), A flow law for dislocation creep of quartz aggregates determined with the molten-salt cell, *Tectonophysics*, *247*, 1–23.

Hempton, M. R. (1987), Constraints on Arabian plate motion and extensional history of the Red Sea, *Tectonics 6*, 687–705.

Hirth, G., and D. Kohlstedt (2003), Rheology of the upper mantle and the mantle wedge: A view from the experimentalists, in *Inside the Subduction Factory*, *Geophys. Monogr. Ser.*, vol. 138, edited by J. Eiler, pp. 83–105, AGU, Washington, D. C., doi:10.1029/138GM06.

Huismans, R. S., and C. Beaumont (2003), Symmetric and asymmetric lithospheric extension: Relative effects of frictional-plastic and viscous strain softening, *J. Geophys. Res.*, *108*(B10), 2496, doi:10.1029/2002JB002026.

Huismans, R., and C. Beaumont (2011), Depth-dependent extension, two-stage breakup and cratonic underplating at rifted margins, *Nature*, *473*, 74–78.

Kameyama, M., D. A. Yuen, and S. I. Karato (1999), Thermal-mechanical effects of low-temperature plasticity (the peierls mechanism) on the deformation of a viscoelastic shear zone, *Earth Planet. Sci. Lett. 168*, 159–172.

Kusznir, N. J., and R. G. Park (1987), The extensional strength of the continental lithosphere: its dependence on geothermal gradient, and crustal composition and thickness, *Geol. Soc. Spec. Publ.*, *28*, 35–52.

Lizarralde, D., et al. (2007), Variation in styles of rifting in the Gulf of California, *Nature*, *448*, 466–469.

Macdonald, D., et al. (2003), Mesozoic break-up of SW Gondwana: Implications for regional hydrocarbon potential of the southern South Atlantic, *Mar. Pet. Geol.*, *20*, 287–308.

McKenzie, D. (1978), Some remarks on the development of sedimentary basins, *Earth Planet. Sci. Lett.*, *40*, 25–32.

Moulin, M., D. Aslanian, and P. Unternehr (2010), A new starting point for the South and Equatorial Atlantic Ocean, *Earth Sci. Rev.*, *98*, 1–37.

Müller, R. D., M. Sdrolias, C. Gaina, and W. R. Roest (2008), Age, spreading rates, and spreading asymmetry of the world's ocean crust, *Geochem. Geophys. Geosyst.*, *9*, Q04006, doi:10.1029/2007GC001743.

Nürnberg, D., and R. D. Müller (1991), The tectonic evolution of the South-Atlantic from late jurassic to present, *Tectonophysics*, *191*, 27–53.

Parsiegla, N., J. Stankiewicz, K. Gohl, T. Ryberg, and G. Uenzelmann-Neben (2009), Southern African continental margin: Dynamic processes of a transform margin, *Geochem. Geophys. Geosyst. 10*, Q03007, doi:10.1029/2008GC002196.

Popov, A. A., and S. V. Sobolev (2008), SLIM3D: A tool for three-dimensional thermo mechanical modeling of lithospheric deformation with elasto-visco-plastic rheology, *Phys. Earth Planet. Interiors 171*, 55–75.

Provost, A., and H. Houston (2003), Stress orientations in northern and central California: Evidence for the evolution of frictional strength along the San Andreas plate boundary system, *J. Geophys. Res. 108*(B3), 2175, doi:10.1029/2001JB001123.

Regenauer-Lieb, K., G. Rosenbaum, and R. F. Weinberg (2008), Strain localisation and weakening of the lithosphere during extension, *Tectonophysics*, *458*, 96–104.

Royden, L., and C. Keen (1980), Rifting process and thermal evolution of the continental margin of eastern Canada determined from subsidence curves, *Earth Planet. Sci. Lett.*, *51*, 343–361.

Schenk, O., and K. Gärtner (2004), Solving unsymmetric sparse systems of linear equations with PARDISO, *Future Generation Comput. Syst.*, *20*, 475–487.

Sibson, R. H. (1974), Frictional constraints on thrust, wrench and normal faults, *Nature*, *249*, 542–544.

Simo, J. C., and T. J. R. Hughes (2000), *Computational Inelasticity*, 2nd ed., Springer, New York.

Sobolev, A. V., S. V. Sobolev, D. V. Kuzmin, K. N. Malitch, and A. G. Petrunin (2009), Siberian meimechites: Origin and relation to flood basalts and kimberlites, *Russ. Geol. Geophys.*, *50*, 999–1033.

Sobolev, S. V., A. Petrunin, Z. Garfunkel, A. Y. Babeyko, and DESERT Group (2005), Thermomechanical model of the Dead Sea transform, *Earth Planet. Sci. Lett.*, *238*, 78–95.

Sobolev, S. V., A. V. Sobolev, D. V. Kuzmin, N. A. Krivolutskaya, A. G. Petrunin, N. T. Arndt, V. A. Radko, and Y. R. Vasiliev (2011), Linking mantle plumes, large igneous provinces and environmental catastrophes, *Nature*, *477*, 312–316.

Sokoutis, D., G. Corti, M. Bonini, J. P. Brun, S. Cloetingh, T. Mauduit, and P. Manetti (2007), Modelling the extension of heterogeneous hot lithosphere, *Tectonophysics*, *444*, 63–79.

Storey, M., J. J. Mahoney, A. D. Saunders, R. A. Duncan, S. P. Kelley, and M. F. Coffin (1995), Timing of hot spot-related volcanism and the break-up of Madagascar and India, *Science*, *267*, 852–855.

Suckro, S. K., K. Gohl, T. Funck, I. Heyde, A. Ehrhardt, B. Schreckenberger, J. Gerlings, V. Damm, and W. Jokat (2012), The crustal structure of southern Baffin Bay: Implications from a seismic refraction experiment, *Geophys. J. Int.*, *190*, 37–58, doi:10.1111/j.1365-246X.2012.05477.x.

Tommasi, A., and A. Vauchez (2001), Continental rifting parallel to ancient collisional belts: An effect of the mechanical anisotropy of the lithospheric mantle, *Earth Planet. Sci. Lett.*, *185*, 199–210.

Torsvik, T. H., S. Rousse, C. Labails, and M. A. Smethurst (2009), A new scheme for the opening of the South Atlantic Ocean and the dissection of an Aptian salt basin, *Geophys. J. Int.*, *177*, 1315–1333.

Tron, V., and J. Brun (1991), Experiments on oblique rifting in brittle-ductile systems, *Tectonophysics*, *188*, 71–84.

Turcotte, D. L., and G. Schubert (2002), *Geodynamics*, 2nd ed., Cambridge Univ. Press, New York.

van Wijk, J. W. (2005), Role of weak zone orientation in continental lithosphere extension, *Geophys. Res. Lett. 32*, L02303, doi:10.1029/2004GL022192.

Weber, M., et al. (2009), Anatomy of the Dead Sea transform from lithospheric to microscopic scale, *Rev. Geophys.*, *47*, RG2002, doi:10.1029/2008RG000264.

Whittaker, J. M., R. D. Müller, G. Leitchenkov, H. Stagg, M. Sdrolias, C. Gaina, and A. Goncharov (2007), Major Australian-Antarctic plate reorganization at Hawaiian-Emperor bend time, *Science*, *318*, 83–86.

Wilks, K. R., and N. L. Carter (1990), Rheology of some continental lower crustal rocks, *Tectonophysics*, *182*, 57–77.

Withjack, M. O., and W. R. Jamison (1986), Deformation produced by oblique rifting, *Tectonophysics*, *126*, 99–124.

Ziegler, P. A., and S. Cloetingh (2004), Dynamic processes controlling evolution of rifted basins, *Earth Sci. Rev. 64*, 1–50.

Zoback, M. D., et al. (1987), New evidence on the state of stress of the San Andreas fault system, *Science*, *238*, 1105–1111.